1   Environmentally dependent dust chemistry of a super Asian dust storm in

2   March 2010: observation and simulation

4   Qiongzhen Wang[1, 2], Xinyi Dong[3], Joshua S. Fu[3], Jian Xu[1], Congrui Deng[1], Yilun

5   Jiang[1], Qingyan Fu[4], Yanfen Lin[4], Kan Huang[1,5]*, Guoshun Zhuang[1]*

6   [1]Center for Atmospheric Chemistry Study, Shanghai Key Laboratory of Atmospheric

7   Particle Pollution and Prevention (LAP3), Department of Environmental Science and

8   Engineering, Fudan University, Shanghai, 200433, P. R. China

9   [2]Environmental Science Research & Design Institute of Zhejiang Province, Hangzhou,

10 310007, P. R. China

11 [3]Department of Civil and Environmental Engineering, University of Tennessee,

12 Knoxville, TN, 37996, USA

13 [4]Shanghai Environmental Monitoring Center, Shanghai, 200030, China

14 [5]Institute of Atmospheric Sciences, Fudan University, Shanghai, 200433, P. R. China

16 Correspondence: huangkan@fudan.edu.cn; gzhuang@fudan.edu.cn

18 **Abstract**

19   Near surface and vertical *in situ* measurements of atmospheric aerosols were

20 conducted in Shanghai during March 19-27, 2010 to explore the transport and

21 chemical evolution of dust aerosols in a super dust storm. An air quality model with

22 optimized physical dust emission scheme and newly implemented dust chemistry was

23 utilized to study the impact of dust chemistry on regional air quality. Two

24 discontinuous dust periods were observed with one travelling over Northern China

25 (DS1) and the other passing over the coastal regions of Eastern China (DS2). Stronger

26 mixing extents between dust and anthropogenic emissions were found in DS2,

27 reflecting by the higher SO_2/PM_{10} and NO_2/PM_{10} ratios as well as typical pollution

28 elemental species such as As, Cd, Pb, and Zn. As a result, the concentrations of SO_4^{2-}

29 and NO_3^- and the ratio of Ca^{2+}/Ca were more elevated in DS2 than in DS1 but

30 opposite for the $[NH_4^+]/[SO_4^{2-}+NO_3^-]$ ratio, suggesting the heterogeneous reactions

31 between calcites and acid gases were significantly promoted in DS2 due to the higher

32 level of relative humidity and gaseous pollution precursors. Lidar observation showed

33 a columnar effect on the vertical structure of aerosol optical properties in DS1 that

34 dust dominantly accounted for ~80-90% of the total aerosol extinction from near the

35 ground to ~700m. In contrast, the dust plumes in DS2 were refrained within lower

36 altitudes while the extinction from spheric particles exhibited maximum at a high

37 altitude of ~800m. The model simulation reproduced relatively consistent results with

38 observations that strong impacts of dust heterogeneous reactions on secondary aerosol

39 formation occurred in areas where the anthropogenic emissions were intensive.

40 Compared to the sulfate simulation, the nitrate formation on dust is suggested to be

41 improved in the future modeling efforts.

42

1. Introduction

44 Asian dust originating from the arid and semiarid areas in Mongolia and China can

45 be transported for long distances, reaching Beijing (Sun et al., 2010), Shanghai (Fu et

46 al., 2010), Xiamen (Zhao et al., 2011), Taiwan (Tsai et al., 2012; Tsai et al., 2014), and

47 even as far as North America (Uno et al., 2009; Wu et al., 2015), exerting significant

48 impacts on the air quality of both densely populated habitations and remote regions.

49 Dust aerosols can significantly influence the regional/global climate directly by

50 absorbing and scattering solar radiation (Bi et al., 2016) and also indirectly by

51 influencing the formation of ice nuclei, cloud, and precipitation (Creamean et al.,

52 2013; Li and Min, 2010; Wang et al., 2010). In addition, deposition of transported

53 dust aerosols into the ocean can enhance phytoplankton blooms due to the existence

54 of bioavailable iron (Wang et al., 2012; Zhuang et al., 1992), which indirectly impacts

55 on global climate change.

56 The effects of dust aerosols on climate change depend critically on their physical

57   and chemical properties. Natural dust aerosols with limited contamination have low

58   light-absorption, with single-scattering albedo of 0.91-0.97 at 500nm and 550nm (Bi

59   et al., 2014; Uchiyama et al., 2005). During the long-range transport, dust aerosols are

60   often modified by their mixing with anthropogenic emissions over the downwind

61   areas (Fischer et al., 2011; Formenti et al., 2011; Huang et al., 2010b; Tobo et al.,

62   2010), resulting in high uncertainties in evaluating the climatic effects of dust aerosols.

63   It was estimated that mineral dust had a radiative forcing of -0.1±0.2 Wm^{-2} (IPCC,

64   2013), of which the uncertainty was as high as 200%. Obviously, the characteristics of

65   dust aerosols and their evolution during the transport are not well understood.

66   In March 2010, a super dust storm swept China, invading extensive areas from

67   Northern China to Southern China including Fujian and Guangdong provinces, and

68   lasting for ~4 days from March 19 to 23 (Li et al., 2011). The dust plumes further

69   extended to the South China Sea (Wang et al., 2011), Taiwan (Tsai et al., 2013), Korea

70   (Tatarov et al., 2012), Japan (Zaizen et al., 2014), and even to North America (Wu et

71   al., 2015). This dust storm was as strong as the one in March 20-21, 2002 and

72   attracted considerable attentions. Lidar observations revealed that this super dust

73   storm was transported within a low altitude (Tatarov et al., 2012; Wang et al., 2011),

74   which could benefit the mixing and interaction between dust aerosols and

75   anthropogenic pollutants. Indeed, modifications of dust aerosols during the transport

76   of this dust storm were suggested based on in situ measurements. Zhao et al. (2011)

77   displayed substantial increases of sulfate and nitrate in aerosols when the dust plumes

78   arrived at Xiamen city of Fujian province, implying the mixing and interaction

79   between dust aerosols and anthropogenic pollutants. Wang et al. (2011) indicated that

80   the dust aerosols detected at the Dongshan Island over the South China Sea were

81   mixed with anthropogenic and marine aerosols. Observations of this dust storm at

82   Tsukuba and Mt. Haruna, Japan showed that most of the transported dust aerosols in

83   lower altitudes were internally mixed with sulfate or seasalt (Zaizen et al., 2014).

84   Most of the studies on this super dust storm focused on investigating the dust

85   aerosols reaching Southeastern China and the South China Sea, and relied on single

86   method, e.g. aerosol chemistry measurement, optical property inversion, or model

87   simulation. In this study, we investigated this super dust storm in Shanghai, a coastal

88   city in Eastern China. A synergy of measurement techniques was applied, including in

89   situ measurements of pollutant gaseous precursors, aerosol with its major chemical

90   components, and Lidar observation of aerosol optical properties. To corroborate the

91   observational evidence, a regional numerical model was used to simulate the impact

92   of dust chemistry on the perturbation of regional air quality. What interested us is that

93   there were two discontinuous dust periods observed in Shanghai with distinctly

94   different transport pathways, providing a great opportunity to study the chemical

95   evolution of transported dust particles under different environmental conditions.

96

97   **2. Methodology**

98   **2.1. Field measurement**

99   **2.1.1. Lidar observation**

100   A dual-wavelength depolarization Lidar (Model:L2S-SMII) developed by the

101   National Institute for Environmental Studies (NIES) of Japan was installed on the roof

102   (~20m above ground level) of a teaching building on the campus of Fudan University

103   in the Yangpu District of Shanghai (Fig. 1b). The Lidar measurement was performed

104   every 15 min (at 00, 15, 30, and 45 minutes every hour) with a height resolution of 6

105   m. Attenuated backscattering coefficient (BSC) and depolarization ratio (DR) of

106   particles at the wavelength of 532 nm were obtained by the measurement. Aerosol

107   extinction coefficients were derived by the Fernald inversion method (Fernald, 1984)

108   with the lidar ratio (extinction-to-backscatter ratio) set as 50 sr (Liu et al., 2002) in the

109   inversion process. The total aerosol extinction coefficient can be split to non-spherical

110   particle (dust particle) and spherical particle (mostly pollution particle) fractions

111   based on the DR of particles. The splitting method was described in detail by

112   Sugimoto et al. (2002) and Shimizu et al. (2004). More details about the Lidar system

113   have been described in Huang et al. (2012).

114

115   **2.1.2. Online particle and gases monitoring**

116   Continuous PM_{10} concentrations were measured by a TEOM (Tapered Element

117   Oscillating Microbalance) 1405D monitor (Thermo Scientific, USA). Trace gases SO_2

118   and NO_2 were measured by a 43i SO_2 analyzer (Thermo Scientific, USA) and a 42i

119   NO-NO_2-NOx analyzer (Thermo Scientific, USA), respectively. All the measured

120   PM_{10} and gases concentrations were averaged and used at intervals of 1hr in this

121   study.

122

123   **2.1.3. Aerosol sampling**

124   TSP (Total Suspended Particles) samples were collected during March 19-27, 2010

125   at the Fudan observational site co-located with all the other instruments. The aerosol

126   samples were collected for 12 hours (normally from 8:00 to 20:00LST (Local

127   Standard Time) in daytime and from 20:00 to 8:00 LST of the next day in nighttime)

128   or 24 hours (normally from 8:00 to 8:00 LST of the next day) on Whatman 41 filters

129   (Whatman Inc., Maidstone, UK) by a medium-volume sampler (Beijing Geological

130   Instrument-Dickel Co., Ltd.; model: TSP/PM_{10}/$PM_{2.5}$-2; flow rate: 77.59 L min^{-1}). All

131   the samples were put in polyethylene plastic bags immediately after sampling and

132   then reserved in a refrigerator. The filters were weighed before and after sampling

133   using an analytical balance (Model: Sartorius 2004MP; reading precision: 10μg) after

134   stabilizing in constant temperature (20±1°C) and humidity (40±2%) for 48 hours. All

135   the procedures were strictly quality controlled to avoid the possible contamination of

136   the samples.

137

138   **2.2. Chemical analysis**

139   **2.2.1. Ion analysis**

140   One fourth of each aerosol sample and blank filters were extracted ultrasonically by

141   10 ml deionized water (18 MΩ cm^{-1}). Inorganic ions of SO_4^{2-}, NO_3^-, Cl^-, Na^+, NH_4^+,

142   K^+, Mg^{2+}, and Ca^{2+} were analyzed by an Ion Chromatography (Dionex ICS 3000,

143   USA) with a separation column of DionexIonpac AS 11, a guard column of Dionex

144   Ionpac AG 11, a self-regenerating suppressed conductivity detector of Dionex Ionpac

145   ED50, and a gradient pump of Dionex Ionpac GP50. The detailed analytical

146   procedures can be found in Yuan et al. (2003).

147

148   **2.2.2. Element analysis**

149   Half of each aerosol sample and blank filters were digested at 170 °C for 4 hours in

150   a high pressure Teflon digestion vessel with 3ml concentrated HNO_3, 1ml

151   concentrated $HClO_4$, and 1 ml concentrated HF. The solutions were dried, and then

152   diluted to 10 ml with deionized water (18 MΩ cm^{-1}). Fifteen elements (Al, As, Ca, Cd,

153   Cu, Fe, Mg, Mn, Na, Ni, Pb, Sr, Ti, V, and Zn) were measured by an inductively

154   coupled plasma optical emission spectroscopy (ICP-OES; SPECTRO, Germany). The

155   detailed analytical procedures were described by Sun et al. (2004a) and Zhuang et al.

156   (2001).

157

158   **2.3. Nation-wide daily PM_{10} data**

159   Air pollution index (API) data in 86 major cities (locations shown in Fig. 1a) over

160   China were obtained from the data center of Ministry of Environmental Protection of

161   China (http://datacenter.mep.gov.cn/). API was converted to PM_{10} concentration

162   according to the following formula:

163    $C = C_{low} + [(I - I_{low})/(I_{high} - I_{low})] \times (C_{high} - C_{low})$,

164   Where C is the concentration of PM_{10} and I is the API value of PM_{10}. I_{high} and I_{low},

165   the two values that the most approaching to value I in the API grading limited value

166   table, stand for the value larger and lower than I, respectively; C_{high} and C_{low} represent

167   the PM_{10} concentration corresponding to I_{high} and I_{low}, respectively. It should be noted

168   that API was recorded with a maximum value of 500, which corresponded to the PM_{10}

169   concentration of 600 μgm^{-3}.

170

171   **2.4. Backward trajectory analysis**

172   48 hours back trajectories of the air masses at both 250 m and 1000 m AGL (Above

173   Ground Level) during dust days starting at Shanghai were computed by the HYSPLIT

174   model (http://ready.arl.noaa.gov/hypub-bin/trajtype.pl?runtype=archive), using the

175   meteorological data of GDAS (1 degree, global, 2006-present). Four trajectories

176   ending at 00, 06, 12, and 18 LST were calculated for each day.

177

178   **2.5. Model simulation**

179   The WRF/CMAQ modeling system was applied to simulate the dust chemistry in

180   this study. The Weather Research and Forecasting model (WRFv3.4) was used to

181   produce the meteorology fields by digesting the reanalysis data from National Centers

182   for Environmental Prediction (NCEP). The Community Multiscale Air Quality

183   Modeling System (CMAQv5.0.1) was configured with the 2005 carbon bond

184   gas-phase mechanism (CB05) and aerosol module AE6. The default CMAQ model

185   doesn't include dust chemistry reactions but only the dust emission module. We have

186   implemented dust chemistry in the CMAQ model and corrected the dust emission

187   module in our earlier work (Dong et al., 2015), which was used to simulate the

188   heterogeneous reactions on dust during the long-range transport in this study. Briefly,

189   the major developments included: (1) The default dust emission module in CMAQ

190   was found to strongly underestimate the dust emissions. By removing the double

191   counting of soil moisture in the default dust emission module and conducting a

192   reanalysis of field data, the threshold friction velocities over various land covers were

193   re-adjusted. (2) The source-dependent speciation profiles of dust particles from the

194   Taklimakan and Gobi Desert were implemented based on field measurement data. (3)

195   Thirteen dust heterogeneous reactions were implemented, including dust reactions

196   with O_3, OH, H_2O_2, CH_3COOH, CH_3OH, CH_2O, HNO_3, N_2O_5, NO_2, NO_3, HO_2, and

197   SO_2. The uptake coefficients of gases onto the surface of dust particles were taken

198   from previous published studies in deserts of China. More details of the technical

199   development of this dust emission and chemistry module in CMAQ and the

200   evaluation of model performance can be found in Dong et al. (2015).

201   The modeling domain includes whole China with a horizontal grid resolution of 36

202   km×36 km and 34 vertical layers with a model top at 50 hPa. The chemical initial and

203   boundary conditions for CMAQ were downscaled from the GEOS-Chem global

204   model. Emissions inputs included anthropogenic emissions from Zhao et al. (2013)

205   over China, biogenic emissions from MEGAN2.1 (Guenther et al., 2006), and

206   biomass burning emissions from FLAMBE (Reid et al., 2009).

207

208   **3. Results and Discussion**

209   **3.1. Spatiotemporal evolution of the 2010 spring dust storm over China**

210   On March 19, 2010, a super dust storm outbroke over the Gobi Desert of Inner

211   Mongolia, China and southern Mongolia. It was driven by a strong cold front and

212   revealed evidently by the OMI (Ozone Monitoring Instrument) aerosol index (AI)

213   from space detection (Tatarov et al., 2012). Along with the cold front, the dust plumes

214   moved southeastward, invading extensive areas from Northern China to Southern

215   China. Fig. 2 shows the daily PM_{10} concentrations over 86 cities of China from March

216   19 to 23, 2010, displaying the spatiotemporal evolution of this dust storm event. On

217   March 20, daily PM_{10} concentrations of higher than 200 μgm^{-3} were observed over

218   widespread areas of Northern China, close to the dust source regions. The PM_{10}

219   concentrations of those heavily polluted cities, including Yinchuan (YC), Datong

220   (DT), Hohhot (HHT), and Beijing (BJ) (red circles in Fig.1a,) reached the threshold of

221   600 μgm^{-3}, the maximum value recorded by API (Fig. 2a). As the dust plumes

222   transported, high levels of PM_{10} started to emerge over Central and Eastern China on

223   March 21, when heavy pollution with daily PM_{10} concentrations higher than

224   420μgm^{-3} were observed over the Yangtze River Delta region as well as in Jiangxi,

225   Hunan, and Hubei provinces. Specifically, the PM_{10} concentrations in Shanghai,

226   Nanjing (NJ), Hefei (HF), Wuhan (WH), Hangzhou (HZ), and so on (blue circles in

227   Fig. 1a) all reached the threshold of 600 μgm^{-3} (Fig. 2c). On March 22 and 23, the

228   dust plumes drifted towards Fujian and Guangdong provinces in Southern China,

229   where PM_{10} concentrations of over 600μgm^{-3} were even observed in coastal cities

230   such as Fuzhou (FZ), Xiamen (XM), and Shantou (ST) (pink circles in Fig.1a). The

231   severe air pollution over China caused by this super dust storm lasted for ~4 days

232   until March 23, resulting in significant impacts on the regional air quality and possible

233   perturbation on regional meteorology.

234

235   **3.2. Identification of two dust plumes with distinct transport pathways**

236   Fig. 3a shows the time-height cross-section of aerosol depolarization ratios (DR)

237   measured at the wavelength of 532 nm from March 19 to 23 in Shanghai. DR of dust

238   particles is higher than pollution particles due to the non-sphericity of dust particles.

239   Thus, aerosol DR is a useful parameter to identify dust events and a threshold value of

240   10% is usually used to distinguish dust from other types of particles (Shimizu et al.,

241   2004). As shown in Fig. 3a, there were evidently two discontinuous periods with

242   aerosol DR higher than 10%, consistent with the two peaks of PM_{10} concentrations

243   measured near the ground (Fig. 4c). The first dust episode (DS1) started from ~16:00

244   LST, March 20 to ~10:00LST, March 21 and the second dust episode (DS2) started

245   from ~6:00 LST, March 22 to ~0:00 LST, March 23.

246   The 48-hours backward trajectories of the air masses during March 20-23 in

247   Shanghai are shown in Fig. 2. It is interesting to note that the transport pathways of

248   the dust plumes in DS1 and DS2 were distinctly different. In DS1, the dust plumes at

249   both low altitudes (i.e. 250m denoted by the black lines in Fig. 2c-d) and high

250   altitudes (i.e. 1000m denoted by the red lines in Fig. 2c-d) were mostly transported

251   from the dust source regions in the Gobi Desert. This is one of the typical inland

252   transport pathways of Asian dust, which passed over Northern China that is

253   characterized of intense anthropogenic emission rates, e.g. from Shanxi, Hebei, and

254   Shandong provinces.

255   In DS2, the air masses reaching Shanghai are shown in Fig. 2e – h. From the

256   starting of DS2 to the midday of March 22 (Fig. 2e-f), the backward trajectories were

257   still mainly from the north but we noticed that the low altitude trajectories which

258   originated from the Gobi Desert travelled over the Yellow Sea and East China Sea

259   and then circled back to Shanghai. After the midday of March 22 (Fig. 2g-h), the

260   trajectories became much shorter and restricted within the costal and offshore areas.

261   The low-altitude trajectories were mainly from the ocean and the high-altitude

262   trajectories shifted from the south. As indicated by the surface observation (Fig. 4a),

263   the southeasterly winds prevailed until ~18:00 LST, March 22 when PM_{10} climbed to

264   reach its peak value in DS2, quite different from DS1 when the northerly winds

265   dominated. The CALIPSO (Cloud-Aerosol Lidar and Infrared Pathfinder Satellite

266   Observations) transect at around 13:00 – 13:30 LST, March 21 specified that the

267   major aerosol type was dust over the East China Sea and South China Sea (Fig. S1).

268   Therefore, it was evident that DS2 passed over the coastal regions of Eastern China

269   and the ocean and it should be a humid dust plume.

270   As visualized in Fig. 3, the two dust plumes were mostly transported at low

271   altitudes below 1km. It is expected that this type of transport would benefit for the

272   mixing and interactions between dust particles and anthropogenic pollutants, as the

273   anthropogenic emissions were mainly trapped within the boundary layer. Transport

274   pathway is one of the most important factors accounting for the evolution of dust

275   particles and the resulting environmental effects (Zaizen et al., 2014; Zhang et al.,

276   2010). In this super dust storm, the two discontinuous dust plumes reaching Shanghai

277   were distinctly different in their transport pathways, providing a great opportunity to

278   study the chemical evolution of dust particles under different transport conditions.

279

280   **3.3. Distinct behaviors of gaseous pollutants between two dust episodes**

281   Fig. 4 illustrates the different behaviors of the two identified dust episodes by

282   plotting the temporal variations of emission precursors (i.e. SO_2 and NO_2) as well as

283   PM_{10} and crucial meteorological parameters. As shown in Fig. 4a, the winds prevailed

284   from the south before the onset of DS1 at ~10:00LST, March 20. During this period,

285   SO_2 and NO_2 concentrations were relatively high with mean concentrations of 39 ± 19

286   and $70\pm25\mu gm^{-3}$, respectively. In the meantime, PM_{10} was at a moderate level of 112

287    $\pm54\mu gm^{-3}$, suggesting the dominance by anthropogenic emissions. It was observed

288   that the peak hourly concentrations of SO_2 and NO_2 up to $97\mu gm^{-3}$ and $116\mu gm^{-3}$

289   occurred just a few hours before the sharp increase of PM_{10}. This was due to that air

290   pollutants north of Shanghai were pushed by the cold front and accumulated before

291   the dust plumes invaded (Guo et al., 2004), which was also evident from the time

292   difference between aerosol backscattering coefficients and depolarization ratios as

293   shown in Fig. 3.

294   From 10:00 LST, March 20 to 11:00 LST, March 21, the winds shifted from the

295   north and northwest accompanied with a quick drop of relative humidity (RH) with a

296   minimum of 25% at 21:00 LST, March 20, indicating the invasion of a strong cold

297   front from Northern China. Correspondingly, PM_{10} abruptly climbed since 16:00 LST

298   and reached $1000\mu gm^{-3}$ (a maximum value of $1000\mu gm^{-3}$ was set in the TEOM

299   1405D monitor) within four hours. This high level of PM_{10} lasted for ~11 hours till

300   04:00 LST, March 21. During this dust episode, the concentrations of SO_2 and NO_2

301   decreased substantially and the lowest values of $17\mu gm^{-3}$ and $27\mu gm^{-3}$ (Fig. 4c) were

302   recorded at 04:00 LST, March 21, due to the strong dilution effect of dust plumes. The

303   ratios of SO_2/PM_{10} and NO_2/PM_{10} were as low as 0.04 ± 0.02 and 0.06 ± 0.03 in DS1

304   compared to that of 0.30 ± 0.05 and 0.57 ± 0.28 before DS1. After 12:00 LST, March

305   21, the wind direction started to shift again from the southeast with an increase of RH.

306   The PM_{10} concentrations quickly decreased below 200 μgm^{-3} within five hours,

307   indicating the pass of the first dust episode over Shanghai.

308   The second wave of dust (DS2) commenced after about half a day as indicated by

309   the temporal variation of PM_{10} climbing quickly since 06:00 LST, March 22. PM_{10}

310   reached its peak of 530 μgm^{-3} observed at ~18:00LST, March 22, much lower than the

311   peak values during DS1. It should be noted that during the growth of DS2 (i.e. from

312   06:00 to 18:00 LST), southerly winds sustained until 18:00 LST, March 22, opposite

313   to DS1. As discussed above, DS2 had gone through the maritime environment during

314   most of its transport trajectory. This can be corroborated by the moderately high RH

315   (Fig. 4b). After 18:00 LST, March 22, PM_{10} underwent a quick decline followed by

316   the prevailing northeast winds and continuously elevated RH. This suggested the sea

317   breezes after 18:00 LST were almost free of dust particles and acted as cleaner for the

318   dust pollution that was previously accumulated. Compared to the mean RH of 46% ±

319   18% in DS1, RH in DS2 was much higher of 69% ± 8%. This was mainly attributed

320   to the different transport pathways of the two dust episodes.

321   One interesting phenomenon that has been rarely observed was that the temporal

322   variations of SO_2 and NO_2 varied fairly consistent with that of PM_{10} in DS2 (Fig. 4c),

323   quite different from DS1 and previous studies (Fu et al., 2010; Guo et al., 2004) that

324   dust usually had a clean effect on the local gaseous pollutants, causing inverse

325   relationship between SO_2/NO_2 and PM_{10}. In this case, NO_2 reached its maximum

326   hourly concentration of 131μgm^{-3} along with the maximum PM_{10} in DS2, the highest

327   during the whole study period. This probably indicated that the dust particles in DS2

328   were externally mixed or "coated" with abundant gaseous pollutants. As a result, the

329   SO_2/PM_{10} and NO_2/PM_{10} ratios reached 0.11 ± 0.03 and 0.20 ± 0.04 in DS2,

330   respectively, much higher than those in DS1 and in a super dust day of April 2, 2007

331   in Shanghai (Fu et al., 2010), revealing that the dust plumes in DS2 were much more

332   polluted.

333   In the following sections, we will investigate deeply into the chemical

334   characteristics and evolution of the two dust episodes.

335

336   **3.4. Chemical evolution of dust aerosols**

3.4.1. Pollution elements significantly enhanced in dust periods

337

338   Table 1 lists the concentrations of measured elements in TSP before, during, and

339 after the two dust episodes in Shanghai. D and N represent the samples that collected

340 in daytime (~8:00 to ~20:00 LST) and nighttime (~20:00 to 8:00 LST in the next day),

341 respectively. NDS represents the non-dust days from March 25 to 27 and the mean

342 concentrations are shown in Table 1. To identify whether these elements were mainly

343 derived from the crustal source or anthropogenic sources, enrichment factors of

344 elements were calculated. Enrichment factor (EF) is defined as

345 $EF = (X/X_{Ref})_{aerosol}/(X/X_{Ref})_{crust}$, where $(X/X_{Ref})_{aerosol}$ is the mass ratio of a given

346 element X to the reference element in aerosol and $(X/X_{Ref})_{crust}$ is the ratio in the crust

347 (Lida, 2006), and Al is the reference element used in this study. EFs of Al, Cu, Ca, Fe,

348 Mg, Na, Mn, Ti, Sr, Ni, and V were calculated to be lower than 5, indicating these

349 eleven elements were mostly from the crustal source, while EFs of As, Cd, Pb, and Zn

350 were higher than 10 even during the dust periods (Fig.5c), indicating these four

351 elements were significantly influenced by anthropogenic sources. Hence, Al, Cu, Ca,

352 Fe, Mg, Na, Mn, Ti, Sr, Ni, and V were classified as "crustal elements" while As, Cd,

353 Pb, and Zn were classified as "pollution elements". Due to the dilution effect of dust

354 plumes, EFs of the four pollution elements decreased from ~100-150 in NDS to

355 ~10-50 in DS1 and ~20-115 in DS2.

356   As shown in Table 1, the concentrations of the crustal elements before the dust

357 event (19N) were as low as those in NDS, but substantially increased in DS1 and DS2,

358 about 3-13 and 1-7 folds of those in NDS, respectively. The highest concentration of

359 Al, widely used as a tracer for dust, reached 67.5 μgm^{-3} in DS1 (20N), comparable to

360 the Al concentration in the super dust day of April 2, 2007 in Shanghai (Fu et al.,

361 2010). The highest concentrations of crustal elements in DS1 (20N) were ~2 folds of

362 those in DS2 (22D), corroborating that the intensity of DS1 was stronger than in DS2.

363   As for the pollution elements, the non-crustal part (nc-) of As, Cd, Pb, and Zn were

364 estimated as $nc\text{-}X = X - Al \times (X/Al)_{crust}$. The concentrations of nc-As, nc-Cd, nc-Pb,

365   and nc-Zn increased in both DS1 and DS2, about 1-4folds of those in NDS (Fig. 5a).

366   As these elements were mainly derived from anthropogenic sources such as coal

367   combustion, industrial processing, vehicle emissions, etc., their enhancement

368   indicated that abundant pollutants had been transported to the downwind regions

369   along with the dust plumes. The mean concentrations of nc-As, nc-Cd, nc-Pb, and

370   nc-Zn were 23.5, 3.6, 154.2, and 580.1 ngm^{-3} in DS2, higher than those of 18.3, 3.1,

371   119.7, and 447.4 ngm^{-3} in DS1, indicating DS2 was more polluted. Consistently, the

372   mass ratios of nc-As, nc-Cd, nc-Pb, and nc-Zn in TSP were 5.1×10^{-3}%, 7.2×10^{-4}%,

373   3.1×10^{-2}%, and 1.2×10^{-1}% in DS2, higher than those of 1.9×10^{-3}%, 3.7×10^{-4}%,

374   1.5×10^{-2}%, and 6.2×10^{-2}% in DS1 (Fig. 5b).

375

376   **3.4.2. Crustal vs. secondary water-soluble ions**

377   Fig. 6 shows the evolution of major water-soluble ions in TSP during the whole

378   dust event. The concentrations of Na$^+$, K$^+$, Mg^{2+}, and Ca^{2+} increased the most among

379   all the ions in both DS1 and DS2 due to their crustal origin, ~2-5 and ~2-3 folds of

380   those in NDS. However, the mass ratios of these ions in TSP generally decreased in

381   the dust periods (Fig. 6d), as the masses of dust particles were dominated by

382   water-insoluble matters. Different from NDS, the concentrations of Ca^{2+} exceeded

383   NH$_4^+$ and ranked as the most abundant cation in the dust periods. This was because

384   Asian dust particles are rich of calcium carbonate (Wang et al., 2005), which could

385   react with acidic nitrogen and sulfur compounds to form Ca(NO$_3$)$_2$ and CaSO$_4$. It has

386   been found Ca-rich particles in Asian dust transported to Japan were mostly in the

387   spherical shape (Zaizenet al., 2014), and many of the spherical Ca-rich particles

388   contained sulfur and nitrogen compounds (Matsuki et al., 2006; Zaizen et al., 2014)

389   due to the heterogeneous reactions. It is noted that the concentrations of Ca^{2+} in DS2

390   were comparable to that in DS1 (Fig. 6b), although the intensity of DS1 was much

391   stronger than DS2. In addition, the mass ratios of Ca^{2+} in TSP were even higher in

392   DS2 than in DS1 (Fig. 6d). Collectively, these results indicated that more calcium in

393   its soluble form was produced via the reactions between calcium carbonate and acids.

394   This could be also revealed by the ratio of Ca^{2+}/Ca that was higher in DS2 (0.2-0.5)

395   than in DS1 (0.1-0.2) (Fig.7a). In DS2, the dust plumes travelled over the ocean and

396   carried higher amount of water vapor as well as SO_2 and NO_2 than DS1 as discussed

397   earlier. In this regard, the heterogeneous reaction between calcium carbonate and

398   acidic gases was enhanced more in DS2, resulting in a higher fraction of calcium

399   carbonate from dust particles that could be transformed to soluble calcium.

400   Cl^- during the dust periods was moderately enhanced by ~1-2 folds compared to

401   NDS, indicating that Cl^- was also impacted by the invasion of dust plumes. As shown

402   in Fig. 6a & 6c, both the concentrations of Cl^- and its mass ratios in TSP were higher

403   in DS2 than in DS1. As the air masses of DS2 passed over the ocean, part of the high

404   Cl^- concentrations should be attributed to the contribution from seasalts. The average

405   equivalent ratio of Cl^- to Na^+ ($[Cl^-]/[Na^+]$) was 1.65 in NDS and 2.17 in 19N, higher

406   than the ratio in seawater (1.17), indicating that anthropogenic sources such as coal

407   combustion (Sun et al., 2014; Yao et al., 2002) contributed significantly to Cl^- in the

408   non-dust days. The $[Cl^-]/[Na^+]$ ratio dropped to ~1.0 in DS1 as massive continental

409   aerosols invaded Shanghai, while in DS2 the ratio was elevated to 1.5. Thus, both

410   seasalts and anthropogenic sources should contribute to the particulate Cl^- in DS2.

411   As for the secondary inorganic ions (i.e. SO_4^{2-}, NO_3^-, and NH_4^+), their

412   concentrations in TSP were elevated to be 16.2, 15.4, and 7.2$\mu g m^{-3}$ in the daytime of

413   March 20 (20D) in DS1. The sampling time of 20D was from ~8:00 to 20:00 LST,

414   including the short period of pollutants accumulation before the arrival of DS1. As a

415   result, the high concentrations of SO_4^{2-} and NO_3^- measured in 20D were contributed

416   from both local and transported sulfate and nitrate, as well as from the heterogeneous

417   reactions on dust particles. In the nighttime of March 20 (20N), the concentrations of

418   NO_3^- and NH_4^+ sharply decreased by 57.8% and 43.2%, respectively. Although SO_4^{2-}

419   also decreased, its reduction extent was much weaker of 27.8% and was still ~2 folds

420   of that in NDS (Fig. 6a). Nitrate formation on dust is strongly dependent on the

421   ambient conditions. Low temperature, low relative humidity, strong wind and low

422   concentrations of pollution gases did not favor the heterogeneous reaction (Huang et

423   al., 2010a; Yuan et al., 2008). Hence, strong dust events usually diluted the

424   concentrations of nitrate (Duvall et al., 2008; Huang et al., 2010a; Wang et al., 2006).

425   As for the sulfate formation on dust, SO_2 could interact with various mineral

426   components of dust particles to produce sulfate, and sulfate became mixed with the

427   dust first competing with nitrate (Dupart et al., 2012; Sullivan et al., 2007). Hence,

428   although the secondary aerosol components were diluted by the invasion of dust, the

429   formation of sulfate could still be compensated by the heterogeneous reaction on dust

430   to some extent.

431   In the daytime of March 22 (22D) during DS2, the concentrations of SO_4^{2-} and

432   NO_3^- reached the highest during the study period with values of 16.6 and 19.3 μgm^{-3},

433   respectively. Although SO_4^{2-} and NO_3^- decreased in the nighttime of March 22 (22N),

434   their levels were still higher than the non-dust days (Fig. 6a). Also, the mass ratios of

435   SO_4^{2-} and NO_3^- in TSP were higher in DS2 than DS1 (Fig. 6c). These results indicated

436   that SO_4^{2-} and NO_3^- were more favorably formed in DS2. It was observed that the

437   concentration of NO_3^- was even higher than that of SO_4^{2-} in both daytime and

438   nighttime samples during DS2, showing a contrary behavior to DS1. As discussed

439   above, the formation of nitrate on dust strongly depends on the ambient conditions.

440   During DS2, RH was at a moderately high level, enhancing the efficiency of aqueous

441   processing on the particles. In addition, the abnormally high concentrations of NO_2

442   (Fig. 4c) suggested the emission precursors were sufficient for the production of

443   nitrate. Finally, high concentrations of nitrate during DS2 may be partially attributed

444   to the reaction between sea salts and nitric acid (Hsu et al., 2014; Huang et al., 2010a)

445   as the dust plumes travelled over the ocean. The formation of secondary aerosol

446   during DS2 should have involved the complex interactions between pollutant

447   precursors, dust, and sea salts.

448   Fig. 7b shows the equivalent ratio of the total anions to the total cations (A/C) in

449   TSP. The A/C ratio dropped to ~0.5 in DS1 from ~0.9 in 19N, which was attributed to

450   the existence of abundant CO_3^{2-} in dust particles that can't be detected by Ion

451   Chromatography (Huang et al., 2010a). The A/C ratio reached 0.85 and 0.80 in 22D

452   and 22N in DS2, respectively, much higher than those in DS1, suggesting that more

453   fraction of $CaCO_3$ in the dust particles in DS2 was transformed to $CaSO_4$ and

454    $Ca(NO_3)_2$ than in DS1, consistent with the higher Ca^{2+}/Ca ratio in DS2 than in DS1

455   (Fig. 7a). The equivalent ratio of NH_4^+ to the sum of SO_4^{2-} and NO_3^- ([NH_4^+]/

456   [SO_4^{2-}+NO_3^-]) in TSP also indicated that the heterogeneous reactions between

457   carbonate and acid gases were more promoted in DS2 compared to DS1. As shown in

458   Fig. 7c, the [NH_4^+]/[SO_4^{2-}+NO_3^-] ratio was slightly higher than one in the non-dust

459   days, indicating that SO_4^{2-} and NO_3^- could be completely neutralized by NH_4^+. In DS1,

460   the [NH_4^+]/[SO_4^{2-}+NO_3^-] ratio was 0.68 and 0.65 in 20D and 20N, while in DS2 it was

461   even lower of 0.45 and 0.55 in 22D and 22N, respectively. Apparently, NH_4^+ was

462   insufficient for completely neutralizing SO_4^{2-} and NO_3^- in both dust episodes,

463   particularly in DS2. The ammonium deficiency was also observed in Kinmen and

464   Zhuhai (Hsu et al., 2014), an island site and a coastal site, respectively, during this

465   super dust storm. We further investigated the [NH_4^++Ca^{2+}]/[SO_4^{2-}+NO_3^-] ratio. As

466   shown in Fig. 7d, with the addition of Ca^{2+}, sulfate and nitrate had been completely

467   neutralized, implying the important role of alkaline calcium as the medium of dust

468   heterogeneous reactions. By estimating the neutralization efficiency of Ca^{2+} (NE_{Ca}) as

469   NE_{Ca} = 1 - [NH_4^+]/[SO_4^{2-}+NO_3^-], the average value of NE_{Ca} in DS1 and DS2 was 0.34

470   and 0.50, respectively. The higher NE_{Ca} in DS2 also suggested the chemical

471   processing via dust was efficient under the environmental conditions such as DS2 in

472   this study.

473

474   **3.5. Vertical evolution of dust particles**

475   In both DS1 and DS2, dust aerosols were mostly refrained below the altitude of

476   1km. Strong vertical gradients of DR and BSC were observed (Fig. 3). To

477 quantitatively investigate the evolution of vertical dust profiles, we selected four

478 typical episodes as follows: 1. 9:00-15:00 LST of March 20: an episode right before

479 the arrival of DS1; 2. 16:00 - 17:45 LST of March 20: an episode before the onset of

480 maximum hourly PM_{10} concentrations in DS1; 3. 18:00 LST of March 20 - 04:45 LST

481 of March 21, an episode that covers the highest PM_{10} concentrations hours

482 (>1000μgm^{-3}) in DS1; 4.6:00 - 18:00 LST of March 22: an episode in DS2.

483   As shown in Fig. 8a, the mean BSC between 9:00 - 15:00LST, March 20 ranged

484 from around 0.005 to 0.02 sr^{-1}km^{-1} from near ground level to 1km. During this period,

485 the mean DR was relatively low of ~ 0.02 - 0.08, suggesting spheric particles, i.e.

486 pollution particles dominated. Accordingly, the contribution of dust to the total

487 extinction was less than 20% (Fig. 8e). As discussed earlier, the high values of light

488 extinction caused by pollution aerosol before the onset of DS1 were due to the

489 pre-accumulation of local and transported pollutants brought by the invaded cold front.

490 On the pathway of DS1 (Fig. 2c), the air masses travelled over large areas with

491 intense anthropogenic emissions and thus a large quantity of pollutants could be

492 pushed to the downstream areas and accumulated before the dust plume arrived.

493   As DS1 invaded, BSC further increased and reached 0.025 sr^{-1}km^{-1} near the surface

494 level (Fig. 8b-c). In the meantime, the values of DR were elevated to be higher than

495 10% from near the ground to ~ 1km (Fig.8f-g). When PM_{10} reached its highest

496 concentrations (>1000μgm^{-3}), the mean DR was ~20-25% extending from near the

497 ground to ~700m (Fig.8g). However, compared to the DR value of ~30–35% for the

498 relatively pure Asian dust (Murayama et al., 2003; Sakai et al., 2003), DR of DS1 was

499 still lower, suggesting the mixing of dust with pollution at a certain extent. As shown

500 in Fig. 8b-c, the extinction coefficient of dust particles obviously overwhelmed that of

501 pollution particles and could be up to 0.82 km^{-1} near the surface level, while that of

502 pollution particles dropped to less than 0.1 km^{-1}. From near the ground to ~700m, no

503 significant vertical gradients of DR and dust ratio (the ratio of the dust extinction in

504 the total extinction of aerosols) were observed. This indicated DS1 had a "top-down"

505   effect on modifying the bulk aerosol optical properties in the lower troposphere in this

506   case. Within this altitude range, dust could account for ~ 80 - 90% of the total aerosol

507   extinction coefficients while only a minor fraction of ~10 - 20% was attributed to the

508   pollution aerosols. Above 700m, DR and the dust ratio quickly deceased, suggesting

509   the impact of dust on the light extinction was much weakened.

510   In DS2, the maximum aerosol BSC and DR averaged between 6:00 and 18:00 LST,

511   March 22 was ~0.015 $sr^{-1}km^{-1}$ and 18%, respectively, observed at an altitude of

512   ~300m. Different from DS1, both DR and the dust ratio had a significant vertical

513   gradient in DS2. As showed in Fig. 8h, DR decreased quickly from its maximum

514   value at ~250m to 5% at ~750m. Correspondingly, the dust ratios decreased from

515   88% to 25%. Moreover, the vertical profiles of dust and pollution extinction

516   coefficients showed distinctly different behaviors during this period. As shown in Fig.

517   8d, the maximum extinction coefficient of dust particles (~0.55 km^{-1}) showed at the

518   altitude of ~250m, while that of pollution particles (~0.25km^{-1}) appeared at a higher

519   altitude of ~800m. As compared to DS1 (Fig. 8b-c), aerosol extinction caused by

520   spheric particles in DS2 showed similar magnitudes below ~ 270m. Above this

521   altitude, aerosol extinction caused by spheric particles in DS2 gradually increased

522   while that in DS1 varied relatively stable with the altitudes. The enhancement of

523   pollution particles in the middle layer during DS2 should be mainly attributed to its

524   unique transport pathway. As shown in Fig. 2e, substantial air masses in the upper

525   layer transported from the south and may bring more moisture. The sounding data at a

526   meteorology station (31.40°N, 121.46°E) in Shanghai supported this statement as

527   shown in Fig. S2.

528   Opposite to the low relative humidity (RH) and its decreasing trend with altitude in

529   DS1, RH in DS2 (measured at 8:00 and 20:00 LST of March 22, respectively) showed

530   much higher values and an increasing trend with altitude (Fig. S2). This phenomenon

531   corroborated our discussions above that the meteorological conditions were more

532   favorable for promoting the dust chemistry in DS2. As a result, the secondary aerosol

533   formation via heterogeneous reaction yielded stronger aerosol extinction in DS2,

534   especially in the middle and upper layers through 270m till the top (2km) where the

535   aerosol extinctions caused by spheric particles were still significant. On the other

536   hand, due to the higher humidity in DS2, the soluble aerosol components should

537   undergo stronger hygroscopic growth and thus partly explain the structure of vertical

538   profile of spheric particles as shown in Fig. 8d. It is commonly regarded that in a dry

539   and less oxidative environment that dust storms are usually associated with, the

540   formation and growth of secondary aerosols are often depressed. However, under

541   certain favorable conditions, new particle formation during dust events could be still

542   discernible (Nie et al., 2014). In this study, vertical profiles of crucial meteorological

543   parameters, pollutant precursors and particle numbers were not available for

544   diagnosing the new particle formation. Tethered balloon-based measurement (Li et al.,

545   2015) could be a good platform for investigating the particle formation during dust

546   events at different altitudes in the future research.

547

548   **3.6 Impact of dust chemistry on regional air quality**

549   Chemical transport modeling (Methods in Section 2.5) was utilized to assess the

550   impact of dust chemistry on the perturbation of air quality at the regional scale. The

551   model performance of CMAQ with improved dust module has been evaluated against

552   various observational datasets and it was demonstrated that the model has relatively

553   good capability in capturing both magnitudes and temporal variability of bulk aerosol

554   (e.g. PM_{10}, AOD) during the spring season over China (Dong et al., 2016). It has to be

555   noted that the model only simulated the aerosol size up to 10 μm while the

556   observation of aerosol chemistry included all the sizes (i.e. TSP), hence the mismatch

557   of size distribution between the model and observation precluded the evaluation of the

558   simulated aerosol chemical species in this study. In the following discussions, we

559   focused on the qualitative assessment of the impact of dust chemistry on the regional

560   air quality.

561   Fig. 9 shows the spatial distribution of simulated mineral aerosols from March 20 –

562   22, 2010, respectively. Accordingly, we show the spatial distribution of Ultraviolet

563   Aerosol Index (UVAI) retrieved from OMI during the same period. UVAI is sensitive

564   to absorbing aerosols, i.e. black carbon and mineral dust (Torres et al., 2007). Hence,

565   the comparison between simulated mineral aerosols and observed UVAI could

566   illustrate how the transport of dust was reproduced. As seen from Fig. 9, high values

567   of UVAI were always observed over the Indo-China Peninsula and this was ascribed

568   to the black carbon aerosols emitted from strong biomass burning over this region

569   during the spring season (Fu et al., 2012; Huang et al., 2013; Tsay et al., 2013). What

570   we concern are the dust and its downwind regions over East Asia. On March 20, high

571   UVAI values stretched from the Gobi Desert to the North China Plain and the Yangtze

572   River Delta. This transport pathway was relatively well reproduced by the model as

573   we can see high concentrations of mineral aerosols over similar areas as well. On the

574   following day of March 21, the satellite observation illustrated the movement of the

575   high UVAI zones further southward and the drifting of dust plumes off the coastline

576   of East China (Fig. 9c). Accordingly, the simulation showed similar behavior with

577   strengthened concentrations of mineral aerosols over the Gobi Desert and downwind

578   areas of the Yangtze River Delta (Fig. 9d). On March 22, although UVAI signals were

579   absent over most areas of East China due to the satellite swath, high UVAI values

580   could still be observed over the tip of the Yangtze River Delta and the East China Sea.

581   This is also relatively consistent with the model simulation that high concentrations of

582   mineral aerosols hovered over the coastlines from YRD to the Taiwan Strait. Overall,

583   we demonstrated that the model is capable of capturing the spatial distribution of dust

584   during the long-range transport.

585   Since we specifically focus on the interaction between dust and anthropogenic

586   pollutants in this study, we have performed two simulations, i.e. one with dust

587   emissions but without dust chemistry and the other one with dust chemistry. The

588   impact of dust chemistry on aerosol chemical components could thus be quantified via

589   the difference between these two simulations. Fig. 10a&c shows the spatial

590   distribution of sulfate via the formation pathway of dust heterogeneous reactions, as

591   well as for nitrate in Fig. 10b&d. Different from the spatial distribution of mineral

592   aerosols (Fig. 9a-c), the formation of sulfate and nitrate via dust chemistry mainly

593   occurred over Northeastern China. This is expected that although the major source

594   region of mineral dust is from the Gobi Desert in Northern China, less anthropogenic

595   emission sources existed there, hence relatively weak atmospheric chemical

596   processing was simulated over the dust source region. On the other hand, drier climate

597   in Northern China also suppressed the extent of heterogeneous reactions on the

598   surface of dust. Hence, the strongest impact from dust heterogeneous reactions on the

599   formation of secondary aerosols occurred in those populous areas where the

600   interaction of anthropogenic precursors and dust was the strongest.

601   As for sulfate, the simulated concentration over Shanghai averaged 8.1, 3.1, and 8.5

602   μgm^{-3} from March 20 – 22, respectively. This temporal variation corresponded to that

603   from observation as discussed in Section 3.4.2. While it has to be noted again that the

604   simulated aerosol species contained particulate sizes less than 10 μm, close match

605   between the simulation and observation was not expected. As we compare DS1 (Fig.

606   10a) and DS2 (Fig. 10c), the simulated sulfate during DS2 was evidently more intense

607   than that during DS1 at a larger geographic region, which was fairly consistent with

608   the observation. Since the daily emission rates digested by the model were almost

609   constant during this period, meteorological conditions should be the determining

610   factor, of which elevated humidity during DS2 has been diagnosed as the most

611   important factor responsible for stronger dust chemistry.

612   As for nitrate, its spatial distribution pattern was as similar as that of sulfate at a

613   certain extent. The simulated concentration of nitrate averaged 3.1, 2.3, and 5.2 μgm^{-3}

614   over Shanghai from March 20 – 22, respectively. Although the simulation results and

615   observational data couldn't be statistically inter-compared due to the size difference as

616   stated above, we think the simulated nitrate should be largely underestimated. The

617   ratio of simulated nitrate between DS2 and DS1 was 1.7, similar to that of ~1.6 from

618   observation. This suggested the favorable meteorological conditions (e.g. higher

619   humidity) on facilitating the dust heterogeneous reaction during DS2 have been

620   accounted by the model. In this regard, we ascribe the low- biased nitrate mainly to

621   several aspects. First, the NOx emissions could have been underestimated. As

622   indicated in Dong et al. (2015) which used the same anthropogenic emission

623   inventory as this study, the model showed some underestimation of the total NO_2

624   columns as compared to the OMI observation, especially over Northeastern China

625   (See Fig. 8 in Dong et al.(2015)). Secondly, HNO_3, N_2O_5, NO_2 and NO_3 were the

626   major precursors of nitrate as implemented in the dust module. Of which, reactions

627   via HNO_3 and N_2O_5 were the dominant pathways of nitrate formation due to their

628   relatively high uptake coefficients on the dust. It was possible that the formation of

629   HNO_3 was underestimated, thus lowering the production of nitrate. However, this is

630   just a guess as observation of gaseous HNO_3 was not available in this study. Lastly,

631   we think the underestimation of nitrate may be due to the omission of nitrate

632   processing on the surface of sea salt, which was especially important for costal cities

633   such as Shanghai (Buseck and Posfai, 1999).

634

635

636   **4. Conclusions**

637   During March 19-23, 2010, a super dust storm swept extensive areas over China

638   from Northern China to Southern China. Two separate dust periods were observed in

639   Shanghai, one from ~16:00 LST, March 20 to ~10:00 LST March 21 (DS1) and the

640   other from ~6:00 LST, March 22 to ~0:00 LST, March 23 (DS2). In DS1, the dust

641   plumes mostly transported over those areas characterized of high pollution emissions

642   in Northern China, while the dust plumes in DS2 transported over the coastal regions

643   of Eastern China with higher RH. The ratios of SO_2/PM_{10} and NO_2/PM_{10} were up to

644   0.11±0.03 and 0.20±0.04 in DS2, much higher than the values in DS1. In addition,

645   the concentrations of typical elemental species such as As, Cd, Pb, and Zn were also

646 more enriched in DS2 than in DS1, indicating the stronger mixing extent between dust

647 and primary anthropogenic emissions in DS2. Due to the higher level of gaseous

648 pollutant precursors associated with moderate relative humidity, SO_4^{2-} and NO_3^-

649 exhibited higher concentrations in DS2 than in DS1. The higher Ca^{2+}/Ca ratio and

650 lower $[NH_4^+]/[SO_4^{2-}+NO_3^-]$ ratio in DS2 suggested the heterogeneous reactions

651 between calcites and acid gases were significantly promoted in DS2. Particularly,

652 more NO_3^- than SO_4^{2-} was formed in DS2, probably due to the high concentrations of

653 NO_2 and the complex reaction among dust, seasalts, and nitric acid. Vertical profiles

654 of aerosol optical properties from Lidar measurement retrieved high depolarization

655 ratios of 20-25% extending from near the ground to ~700m in DS1 and it was

656 estimated that dust dominantly accounted for ~80-90% of the total aerosol extinction.

657 In DS2, the vertical structure of aerosol changed dramatically from that of DS1. The

658 maximum extinction coefficient of dust particles emerged at the altitude of ~250m in

659 DS2, while that of pollution particles showed at a higher altitude of ~800m. The

660 abnormal increase of humidity as a function of altitude from the southerly winds

661 explained this phenomenon due to promoted heterogeneous reactions on dust particles

662 and the subsequent aerosol hygroscopic growth.

663 Simulated mineral aerosols were compared to the remote sensing UVAI from

664 satellite, showing consistent spatial patterns between model and observation. By

665 applying the dust scheme with explicit chemistry mechanisms, evident impacts of dust

666 heterogeneous reactions on secondary aerosol formation were reproduced over

667 widespread areas of Northeastern China where the anthropogenic emissions were

668 intensive. The sulfate formation was relatively well simulated while the nitrate

669 formation on dust was believed to be largely underestimated. More research on

670 laboratory kinetic studies of nitrate dust chemistry is suggested. Also, the feedback

671 between dust chemistry and regional climate change needs to be investigated in the

672 future.

673

674   **Acknowledgment**

675   This work was supported by the National Natural Science Foundation of China

676   (Nos. 41405115, 41429501, and 91644105) and National Key Technology Research

677   and Development Program of the Ministry of Science and Technology of China (No.

678   2014BAC22B06). Dr. Qingyan Fu and Yanfen Lin would like to acknowledge support

679   from Shanghai Science and Technology Fund (Nos. 14DZ1202900 and 16DZ1204601)

680   and National Key Technology Research and Development Program of the Ministry of

681   Science and Technology of China (No. 2014BAC22B00).

682

683   **References:**
684   Bi, J., Huang, J., Holben, B., 2016. Comparison of key absorption and optical
685   properties between pure and transported anthropogenic dust over East and Central
686   Asia. 1-37.
687   Bi, J., Shi, J., Xie, Y., 2014. Dust Aerosol Characteristics and Shortwave Radiative
688   Impact at a Gobi Desert of Northwest China during the Spring of 2012. Journal of the
689   Meteorological Society of Japan 92, 33-56.
690   Buseck, P., Posfai, M., 1999. Airborne minerals and related aerosol particles: Effects
691   on climate and the environment. Proc. Natl. Acad. Sci. U. S. A., 3372–3379, doi:
692   10.1073/pnas.96.7.3372.
693   Creamean, J.M., Suski, K.J., Rosenfeld, D., Cazorla, A., Demott, P.J., Sullivan, R.C.,
694   White, A.B., Ralph, F.M., Minnis, P., Comstock, J.M., 2013. Dust and biological
695   aerosols from the Sahara and Asia influence precipitation in the western U.S. Science
696   339, 1572.
697   Dong, X., Fu, J.S., Huang, K., Tong, D., Zhuang, G., 2015. Model development of
698   dust emission and heterogeneous chemistry within the Community Multiscale Air
699   Quality modeling system and its application over East Asia. Atmospheric Chemistry
700   & Physics 15, 35591-35643.
701   Dupart, Y., King, S.M., Nekat, B., Nowak, A., Wiedensohler, A., Herrmann, H., David,
702   G., Thomas, B., Miffre, A., Rairoux, P., 2012. Mineral dust photochemistry induces
703   nucleation events in the presence of SO2. Proc Natl Acad Sci U S A 109,
704   20842-20847.
705   Duvall, R.M., Majestic, B.J., Shafer, M.M., Chuang, P.Y., Simoneit, B.R.T., Schauer,
706   J.J., 2008. The water-soluble fraction of carbon, sulfur, and crustal elements in Asian
707   aerosols and Asian soils. Atmospheric Environment 42, 5872-5884.
708   Fernald, F.G., 1984. Analysis of atmospheric lidar observations: some comments.
709   Applied Optics 23, 652.
710   Fischer, E.V., Perry, K.D., Jaffe, D.A., 2011. Optical and chemical properties of
711   aerosols transported to Mount Bachelor during spring 2010. Journal of Geophysical

712   Research-Atmospheres 116, 13.

713   Formenti, P., Schutz, L., Balkanski, Y., Desboeufs, K., Ebert, M., Kandler, K., Petzold,
714   A., Scheuvens, D., Weinbruch, S., Zhang, D., 2011. Recent progress in understanding
715   physical and chemical properties of African and Asian mineral dust. Atmospheric
716   Chemistry and Physics 11, 8231-8256.

717   Fu, J.S., Hsu, N.C., Gao, Y., Huang, K., Li, C., Lin, N.H., Tsay, S.C., 2012. Evaluating
718   the influences of biomass burning during 2006 BASE-ASIA: a regional chemical
719   transport modeling. Atmospheric Chemistry & Physics 12, 5271-5273.

720   Fu, Q.Y., Zhuang, G.S., Li, J.A., Huang, K., Wang, Q.Z., Zhang, R., Fu, J., Lu, T.,
721   Chen, M., Wang, Q.A., Chen, Y., Xu, C., Hou, B., 2010. Source, long-range transport,
722   and characteristics of a heavy dust pollution event in Shanghai. Journal of
723   Geophysical Research-Atmospheres 115, -.

724   Guenther, A., Karl, T., Harley, P., Wiedinmyer, C., Palmer, P.I., Geron, C., 2006.
725   Estimates of global terrestrial isoprene emissions using MEGAN (Model of Emissions
726   of Gases and Aerosols from Nature). Atmospheric Chemistry & Physics 6, 3181-3210.

727   Guo, J., Rahn, K.A., Zhuang, G.S., 2004. A mechanism for the increase of pollution
728   elements in dust storms in Beijing. Atmospheric Environment 38, 855-862.

729   Hsu, S.-C., Lee, C.S.L., Huh, C.-A., Shaheen, R., Lin, F.-J., Liu, S.C., Liang, M.-C.,
730   Tao, J., 2014. Ammonium deficiency caused by heterogeneous reactions during a
731   super Asian dust episode. Journal of Geophysical Research: Atmospheres 119,
732   2013JD021096.

733   Huang, K., Fu, J.S., Hsu, N.C., Gao, Y., Dong, X., Tsay, S.C., Yun, F.L., 2013. Impact
734   assessment of biomass burning on air quality in Southeast and East Asia during
735   BASE-ASIA. Atmospheric Environment 78, 291-302.

736   Huang, K., Zhuang, G., Lin, Y., Fu, J.S., Wang, Q., Liu, T., Zhang, R., Jiang, Y., Deng,
737   C., Fu, Q., Hsu, N.C., Cao, B., 2012. Typical types and formation mechanisms of haze
738   in an Eastern Asia megacity, Shanghai. Atmos. Chem. Phys. 12, 105-124.

739   Huang, K., Zhuang, G.S., Li, J.A., Wang, Q.Z., Sun, Y.L., Lin, Y.F., Fu, J.S., 2010a.
740   Mixing of Asian dust with pollution aerosol and the transformation of aerosol
741   components during the dust storm over China in spring 2007. Journal of Geophysical
742   Research-Atmospheres 115, -.

743   Huang, K., Zhuang, G.S., Lin, Y.F., Li, J.A., Sun, Y.L., Zhang, W.J., Fu, J.S., 2010b.
744   Relation between optical and chemical properties of dust aerosol over Beijing, China.
745   Journal of Geophysical Research-Atmospheres 115, -.

746   IPCC, 2013. Climate Change 2013: The Physical Science Basiss, Contribution of
747   Working Group I to the Fifth Assessment Report of the Intergovenmental Panel on
748   Climate Change. Cambridge University Press, New York, USA.

749   Li, J., Fu, Q., Huo, J., Wang, D., Yang, W., Bian, Q., Duan, Y., Zhang, Y., Pan, J., Lin,
750   Y., Huang, K., Bai, Z., Wang, S.-H., Fu, J.S., Louie, P.K.K., 2015. Tethered
751   balloon-based black carbon profiles within the lower troposphere of Shanghai in the
752   2013 East China smog. Atmospheric Environment 123, Part B, 327-338.

753   Li, J.W., Han, Z.W., Zhang, R.J., 2011. Model study of atmospheric particulates

754   during dust storm period in March 2010 over East Asia. Atmospheric Environment 45,
755   3954-3964.
756   Li, R., Min, Q.L., 2010. Impacts of mineral dust on the vertical structure of
757   precipitation. Journal of Geophysical Research-Atmospheres 115, 14.
758   Lida, D.R., 2006. Handbook of Chemistry and Physics: A Ready-Reference Book of
759   Chemical and Physical Data. 86th ed. CRC Press, New York, 14-17.
760   Liu, Z.Y., Sugimoto, N., Murayama, T., 2002. Extinction-to-backscatter ratio of Asian
761   dust observed with high-spectral-resolution lidar and Raman lidar. Applied Optics 41,
762   2760-2767.
763   Matsuki, A., Iwasaka, Y., Shi, G., Zhang, D., Trochkine, D., Yamada, M., Kim, Y.S.,
764   Chen, B., Nagatani, T., Miyazawa, T., 2006. Morphological and chemical
765   modification of mineral dust: Observational insight into the heterogeneous uptake of
766   acidic gases. Geophysical Research Letters 32, 312-329.
767   Murayama, T., Masonis, S.J., Redemann, J., Anderson, T.L., Schmid, B., Livingston,
768   J.M., Russell, P.B., Huebert, B., Howell, S.G., Mcnaughton, C.S., 2003. An
769   intercomparison of lidar-derived aerosol optical properties with airborne
770   measurements near Tokyo during ACE-Asia. Journal of Geophysical Research
771   Atmospheres 108, 8561.
772   Nie, W., Ding, A., Wang, T., Kerminen, V.-M., George, C., Xue, L., Wang, W., Zhang,
773   Q., Petäjä, T., Qi, X., Gao, X., Wang, X., Yang, X., Fu, C., Kulmala, M., 2014.
774   Polluted dust promotes new particle formation and growth. Sci Rep-Uk 4, 6634.
775   Reid, J.S., Hyer, E.J., Prins, E.M., Westphal, D.L., Zhang, J., Wang, J., Christopher,
776   S.A., Curtis, C.A., Schmidt, C.C., Eleuterio, D.P., 2009. Global Monitoring and
777   Forecasting of Biomass-Burning Smoke: Description of and Lessons From the Fire
778   Locating and Modeling of Burning Emissions (FLAMBE) Program. IEEE Journal of
779   Selected Topics in Applied Earth Observations & Remote Sensing 2, 144-162.
780
781   Sakai, T., Nagai T., Nakazato M., Mano Y., and Matsumura T., 2003. Ice clouds and
782   Asian dust studied with lidar measurements of particle extinction-to-backscatter ratio,
783   particle depolarization, and water-vapor mixing ratio over Tsukuba, Applied Optics 42,
784   7103–7116.
785   Shimizu, A., Sugimoto, N., Matsui, I., Arao, K., Uno, I., Murayama, T., Kagawa, N.,
786   Aoki, K., Uchiyama, A., Yamazaki, A., 2004. Continuous observations of Asian dust
787   and other aerosols by polarization lidars in China and Japan during ACE-Asia. Journal
788   of Geophysical Research: Atmospheres 109, D19S17.
789   Sugimoto, N., Matsui, I., Shimizu, A., Uno, I., Asai, K., Endoh, T., Nakajima, T., 2002.
790   Observation of dust and anthropogenic aerosol plumes in the Northwest Pacific with a
791   two-wavelength polarization lidar on board the research vessel Mirai. Geophysical
792   Research Letters 29.
793   Sullivan, R.C., Guazzotti, S.A., Sodeman, D.A., Prather, K.A., 2007. Direct
794   observations of the atmospheric processing of Asian mineral dust. Atmospheric
795   Chemistry & Physics 7, 1213-1236.

796   Sun, Y.L., Jiang, Q., Wang, Z.F., Fu, P.Q., Li, J., Yang, T., Yin, Y., 2014. Investigation
797   of the sources and evolution processes of severe haze pollution in Beijing in January
798   2013. J Geophys Res-Atmos 119, 4380-4398.
799   Sun, Y.L., Zhuang, G.S., Huang, K., Li, J.A., Wang, Q.Z., Wang, Y., Lin, Y.F., Fu, J.S.,
800   Zhang, W.J., Tang, A.H., Zhao, X.J., 2010. Asian dust over northern China and its
801   impact on the downstream aerosol chemistry in 2004. Journal of Geophysical
802   Research-Atmospheres 115, -.
803   Sun, Y.L., Zhuang, G.S., Ying, W., Han, L.H., Guo, J.H., Mo, D., Zhang, W.J., Wang,
804   Z.F., Hao, Z.P., 2004. The air-borne particulate pollution in Beijing - concentration,
805   composition, distribution and sources. Atmospheric Environment 38, 5991-6004.
806   Tatarov, B., Muller, D., Noh, Y.M., Lee, K.H., Shin, D.H., Shin, S.K., Sugimoto, N.,
807   Seifert, P., Kim, Y.J., 2012. Record heavy mineral dust outbreaks over Korea in 2010:
808   Two cases observed with multiwavelength aerosol/depolarization/Raman-quartz lidar.
809   Geophysical Research Letters 39, 5.
810   Tobo, Y., Zhang, D.Z., Matsuki, A., Iwasaka, Y., 2010. Asian dust particles converted
811   into aqueous droplets under remote marine atmospheric conditions. Proc. Natl. Acad.
812   Sci. U. S. A. 107, 17905-17910.
813   Torres, O., Tanskanen, A., Veihelmann, B., Ahn, C., Braak, R., Bhartia, P.K., Veefkind,
814   P., Levelt, P., 2007. Aerosols and surface UV products from Ozone Monitoring
815   Instrument observations: An overview. J Geophys Res-Atmos 112.
816   Tsai, J-H T,Huang K-L, Lin, N-H, Chen, S-J, Lin, T-Chang, Chen, S-C, Lin, C.-C.,
817   Hsu, S.-C., Lin, W.-Y., 2012. Influence of an Asian Dust Storm and Southeast Asian
818   Biomass Burning on the Characteristics of Seashore Atmospheric Aerosols in
819   Southern Taiwan. Aerosol & Air Quality Research 12, 1105-1115.
820   Tsai, F., Tu, J.-Y., Hsu, S.-C., Chen, W.-N., 2014. Case study of the Asian dust and
821   pollutant event in spring 2006: Source, transport, and contribution to Taiwan. Science
822   of the Total Environment 478, 163-174.
823   Tsai, F.J., Fang, Y.S., Huang, S.J., 2013. CASE STUDY OF ASIAN DUST EVENT
824   ON MARCH 19-25, 2010 AND ITS IMPACT ON THE MARGINAL SEA OF
825   CHINA. J. Mar. Sci. Technol.-Taiwan 21, 353-360.
826   Tsay, S.C., Hsu, N.C., Lau, K.M., Li, C., Gabriel, P.M., Ji, Q., Holben, B.N., Welton,
827   E.J., Nguyen, A.X., Janjai, S., 2013. From BASE-ASIA toward 7-SEAS: A
828   satellite-surface perspective of boreal spring biomass-burning aerosols and clouds in
829   Southeast Asia. Atmospheric Environment 78, 20-34.
830   Uchiyama, A., Yamazaki, A., Togawa, H., Asano, J., Shi, G., 2005. Single Scattering
831   Albedo of Aeolian Dust as Inferred from Sky-radiometer and in situ Ground-based
832   Measurement. Scientific Online Letters on the Atmosphere Sola 1, 209-212.
833   Uno, I., Eguchi, K., Yumimoto, K., Takemura, T., Shimizu, A., Uematsu, M., Liu, Z.Y.,
834   Wang, Z.F., Hara, Y., Sugimoto, N., 2009. Asian dust transported one full circuit
835   around the globe. Nature Geoscience 2, 557-560.
836   Wang, S.-H., Hsu, N.C., Tsay, S.-C., Lin, N.-H., Sayer, A.M., Huang, S.-J., Lau,
837   W.K.M., 2012. Can Asian dust trigger phytoplankton blooms in the oligotrophic

838   northern South China Sea? Geophysical Research Letters 39, L05811.

839   Wang, S.H., Lin, N.H., OuYang, C.F., Wang, J.L., Campbell, J.R., Peng, C.M., Lee,
840   C.T., Sheu, G.R., Tsay, S.C., 2010. Impact of Asian dust and continental pollutants on
841   cloud chemistry observed in northern Taiwan during the experimental period of
842   ABC/EAREX 2005. Journal of Geophysical Research-Atmospheres 115, -.

843   Wang, S.H., Tsay, S.C., Lin, N.H., Hsu, N.C., Bell, S.W., Li, C., Ji, Q., Jeong, M.J.,
844   Hansell, R.A., Welton, E.J., Holben, B.N., Sheu, G.R., Chu, Y.C., Chang, S.C., Liu,
845   J.J., Chiang, W.L., 2011. First detailed observations of long-range transported dust
846   over the northern South China Sea. Atmospheric Environment 45, 4804-4808.

847   Wang, Y., Zhuang, G.S., Sun, Y., An, Z.S., 2005. Water-soluble part of the aerosol in
848   the dust storm season - evidence of the mixing between mineral and pollution aerosols.
849   Atmospheric Environment 39, 7020-7029.

850   Wang, Y., Zhuang, G.S., Sun, Y.L., An, Z.S., 2006. The variation of characteristics and
851   formation mechanisms of aerosols in dust, haze, and clear days in Beijing.
852   Atmospheric Environment 40, 6579-6591.

853   Wu, Y., Han, Z., Nazmi, C., Gross, B., Moshary, F., 2015. A trans-Pacific Asian dust
854   episode and its impacts to air quality in the east coast of U.S. Atmospheric
855   Environment 106, 358-368.

856   Yao, X., Chan, C.K., Fang, M., Cadle, S., Chan, T., Mulawa, P., He, K., Ye, B., 2002.
857   The water-soluble ionic composition of PM2.5 in Shanghai and Beijing, China.
858   Atmospheric Environment 36, 4223-4234.

859   Yuan, H., Wang, Y., Zhuang, G., 2003. The simultaneous determination of organic
860   acid, MSA with inorganic anions in aerosol and rainwater by ion chromatography (in
861   Chinese). Journal of   Instrument   Analalysis 6, 6-12.

862   Yuan, H., Zhuang, G.S., Li, J., Wang, Z.F., Li, J., 2008. Mixing of mineral with
863   pollution aerosols in dust season in Beijing: Revealed by source apportionment study.
864   Atmospheric Environment 42, 2141-2157.

865   Zaizen, Y., Naoe, H., Takahashi, H., Okada, K., 2014. Modification of Asian-dust
866   particles transported by different routes – A case study. Atmospheric Environment 97,
867   435-446.

868   Zhang, W.J., Zhuang, G.S., Huang, K., Li, J.A., Zhang, R., Wang, Q.Z., Sun, Y.L., Fu,
869   J.S., Chen, Y., Xu, D.Q., Wang, W., 2010. Mixing and transformation of Asian dust
870   with pollution in the two dust storms over the northern China in 2006. Atmospheric
871   Environment 44, 3394-3403.

872   Zhao, B., Wang, S., Dong, X., Wang, J., Duan, L., Fu, X., Hao, J., Fu, J., 2013.
873   Environmental effects of the recent emission changes in China: implications for
874   particulate matter pollution and soil acidification. Environmental Research Letters 8,
875   024031.

876   Zhao, J., Zhang, F., Xu, Y., Chen, J., Yin, L., Shang, X., Xu, L., 2011. Chemical
877   Characteristics of Particulate Matter during a Heavy Dust Episode in a Coastal City,
878   Xiamen, 2010. Aerosol & Air Quality Research 11, 300-309.

879   Zhuang, G.S., Guo, J.H., Yuan, H., Zhao, X.J., 2001. The compositions, sources, and

880   size distribution of the dust storm from China in spring of 2000 and its impact on the
881   global environment. Chinese Science Bulletin 46, 895-901.
882   Zhuang, G.S., Yi, Z., Duce, R.A., Brown, P.R., 1992. Link between Iron and Sulfur
883   Cycles Suggested by Detection of Fe(Ii) in Remote Marine Aerosols. Nature 355,
884   537-539.

885 Table 1 Concentrations of the measured elements (μg/m³) in TSP before, during, and
886 after the dust periods from March 19 to 22 and in non-dust days (NDS) in Shanghai.
887 N, D, and NDS represent the nighttime samples collected from 20:00 to 8:00 in the
888 next day, the daytime samples collected from 8:00 to 20:00, and the average of the
889 non-dust samples collected from March 25 to 27, respectively.
890
891

	DS1					DS2		
	19 N	20 D	20 N	21 D	21 N	22 D	22 N	NDS
TSP	168.5	605.0	1306.7	155.1	194.3	683.3	348.2	160.5
Al	6.2	36.4	67.5	9.6	9.3	35.8	12.8	5.2
Ca	8.5	37.3	56.9	9.4	8.6	33.2	12.0	8.0
Fe	3.2	23.3	42.1	6.8	6.0	23.7	11.6	4.2
Mg	1.4	9.5	14.4	2.2	2.3	8.1	3.4	1.4
Na	1.3	7.9	19.1	2.8	3.9	7.9	3.5	2.4
Mn	0.2	1.0	2.2	0.4	0.3	1.1	0.6	0.2
Ti	0.2	1.9	4.3	0.6	0.5	1.9	0.7	0.3
Sr	4.3×10^{-2}	1.6×10^{-1}	3.3×10^{-1}	4.8×10^{-2}	4.3×10^{-2}	1.9×10^{-1}	6.4×10^{-2}	3.8×10^{-2}
V	1.5×10^{-2}	5.2×10^{-2}	1.0×10^{-1}	1.7×10^{-2}	1.5×10^{-2}	4.7×10^{-2}	2.7×10^{-2}	1.3×10^{-2}
Ni	6.7×10^{-3}	2.5×10^{-2}	4.6×10^{-2}	1.1×10^{-2}	3.0×10^{-3}	2.8×10^{-2}	1.6×10^{-2}	6.5×10^{-3}
Zn	7.5×10^{-1}	6.5×10^{-1}	3.4×10^{-1}	1.9×10^{-1}	2.3×10^{-1}	6.3×10^{-1}	5.7×10^{-1}	4.0×10^{-1}
Pb	1.3×10^{-1}	1.5×10^{-1}	1.1×10^{-1}	4.0×10^{-2}	3.7×10^{-2}	2.0×10^{-1}	1.2×10^{-1}	8.6×10^{-2}
Cu	1.3×10^{-2}	6.3×10^{-2}	7.2×10^{-2}	4.0×10^{-2}	2.4×10^{-2}	6.1×10^{-2}	4.7×10^{-2}	3.7×10^{-2}
As	1.2×10^{-2}	1.3×10^{-2}	2.6×10^{-2}	9.2×10^{-3}	1.3×10^{-2}	2.5×10^{-2}	2.4×10^{-2}	1.1×10^{-2}
Cd	2.8×10^{-3}	3.1×10^{-3}	3.4×10^{-3}	7.4×10^{-4}	1.2×10^{-3}	4.7×10^{-3}	2.7×10^{-3}	1.3×10^{-3}

892

893

894
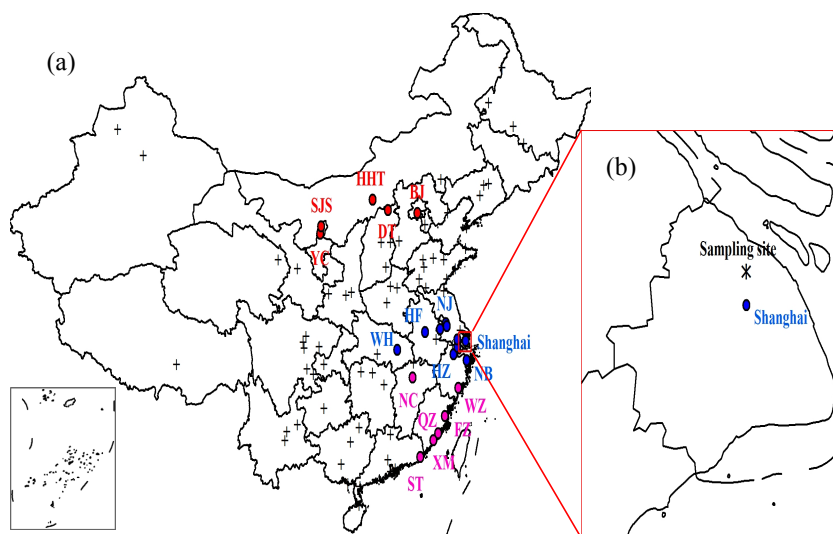
895
896
897
898
899
900 Fig.1 (a) Locations of the 86 major cities over China. The cities with PM_{10}
901 concentrations up to 600μgm^{-3} on March 20, 21, and 22 were marked by red, blue,
902 and pink circles, respectively. (b) The site location of the ground-based measurement
903 in Shanghai.

904
905
906
907
908
909
910
911
912
913
914
915
916
917
918
919
920
921

922
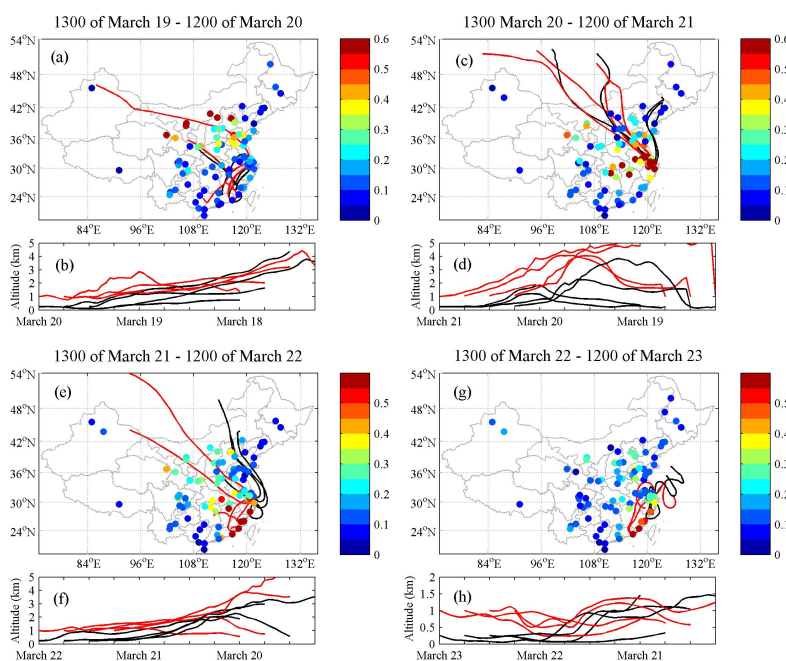
923
924

925 Fig.2 Daily PM$_{10}$ concentrations (mg m^{-3}) in 86 major cities over China and 48 hours
926 backward trajectories of the air masses at both 250m (black lines) and 1000m (red
927 lines) above ground level over Shanghai during March 19-23, 2010. Four trajectories
928 ending at 00, 06, 12, and 18 LST are computed for each day.

929
930
931
932
933
934
935
936
937
938
939
940
941
942
943
944
945

946

947

948
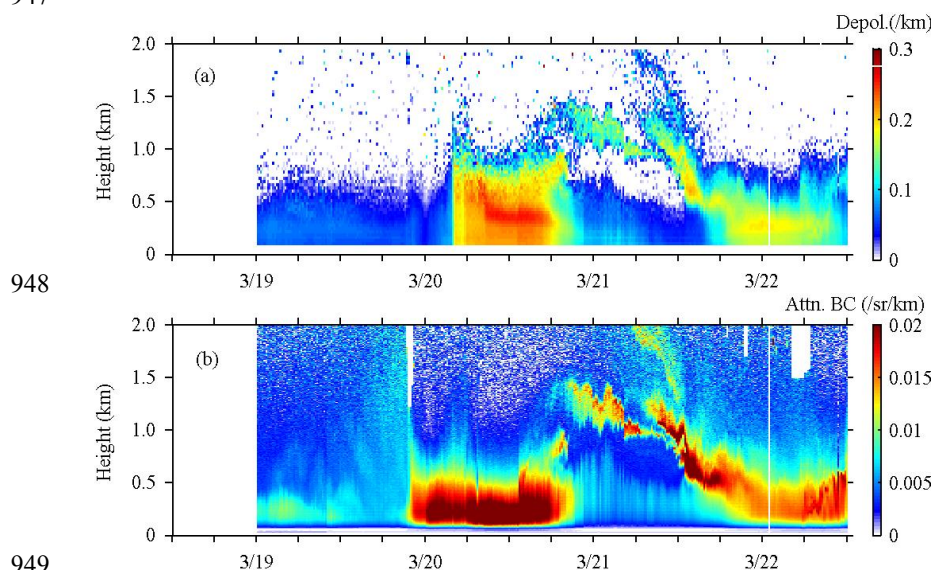
949

950

951 Fig.3 Time-height cross-section of (a) depolarization ratios and (b) attenuated aerosol

952 backscattering coefficients measured by a Lidar at the wavelength of 532 nm during

953 March 19-22, 2010.

954

955

956

957

958

959

960

961

962

963

964

965

966

967

968

969
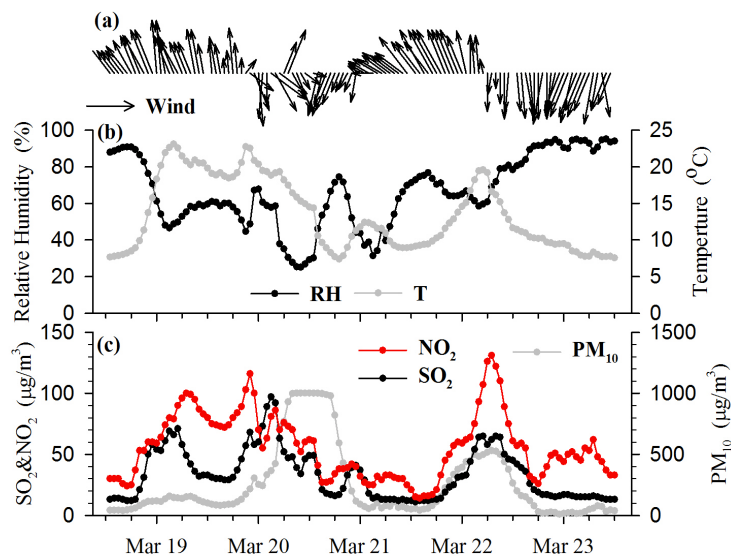
970

971 Fig.4 Time-series of PM$_{10}$, SO$_2$, NO$_2$, and meteorological factors including wind
972 conditions, relative humidity (RH), and ambient temperature (T) in Shanghai during
973 March 19-23, 2010.

974

975

976

977

978

979

980

981

982

983

984

985

986

987

988

989

990

991

992

993

994

995
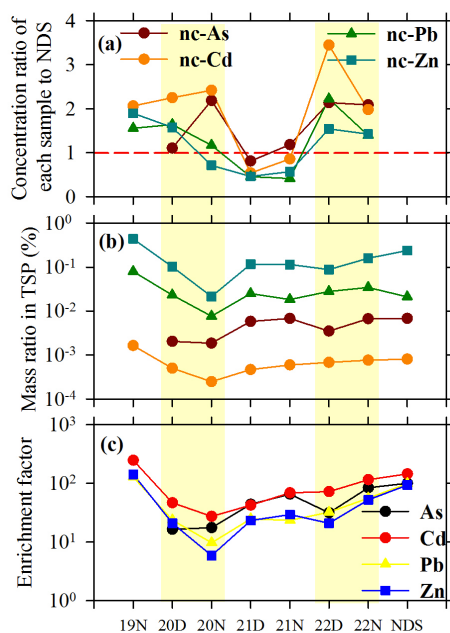
Fig.5 Variations of (a) the mass concentration ratio of each sample to the NDS sample
for nc-As, nc-Cd, nc-Pb, and nc-Zn, (b) the mass ratios, and (c) enrichment factors of
pollution elements As, Cd, Pb, and Zn in TSP during March 19-22 and non-dust days
(NDS). D, N, and NDS represent the daytime samples collected from 8:00 to 20:00
LST, the nighttime samples collected from 20:00 to 8:00 LST in the next day, and the
average of the non-dust samples collected from March 25 to 27, respectively.

1002
1003
1004
1005
1006
1007
1008
1009
1010
1011
1012
1013
1014
1015

1016
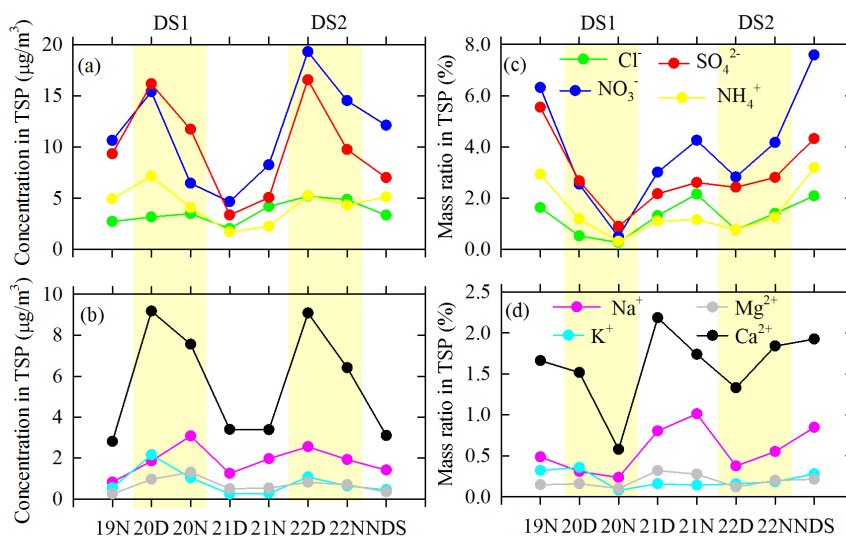
1017
1018
1019 Fig.6 Variations of the concentrations of water-soluble ions and their mass ratios in
1020 TSP during March 19-22 and NDS, 2010.
1021
1022
1023
1024
1025
1026
1027
1028
1029
1030
1031
1032
1033
1034
1035
1036
1037
1038
1039
1040
1041

1042
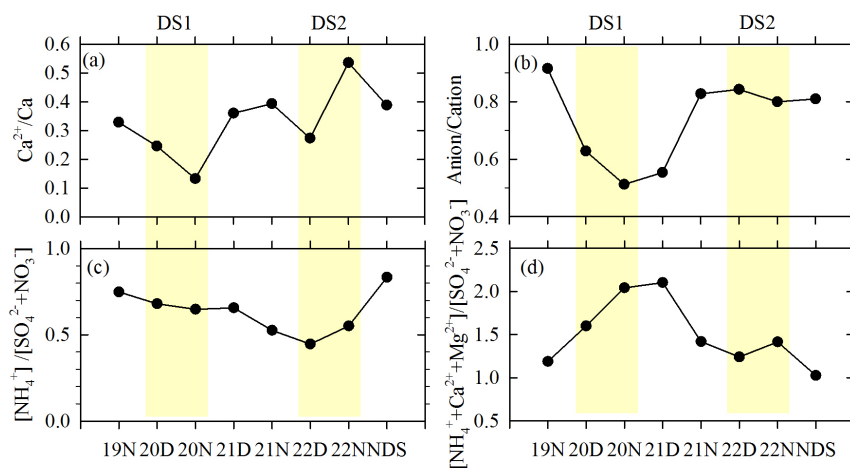
1043
1044
1045 Fig.7 Variations of (a) the ratios of Ca^{2+}/Ca, (b) the equivalent concentrations of the
1046 total anions to the total cations (Anion/Cation), (c) the equivalent concentrations of
1047 NH_4^+ to the sum of SO_4^{2-} and NO_3^- ($[NH_4^+]/[SO_4^{2-}+NO_3^-]$), and (d) the equivalent
1048 concentrations of the sum of NH_4^+, Ca^{2+}, and Mg^{2+} to the sum of SO_4^{2-} and NO_3^-
1049 ($[NH_4^++ Ca^{2+}+ Mg^{2+}]/[SO_4^{2-}+NO_3^-]$) in TSP during March 19-22 and NDS, 2010.
1050
1051
1052
1053
1054
1055
1056
1057
1058
1059
1060
1061
1062
1063
1064
1065
1066
1067
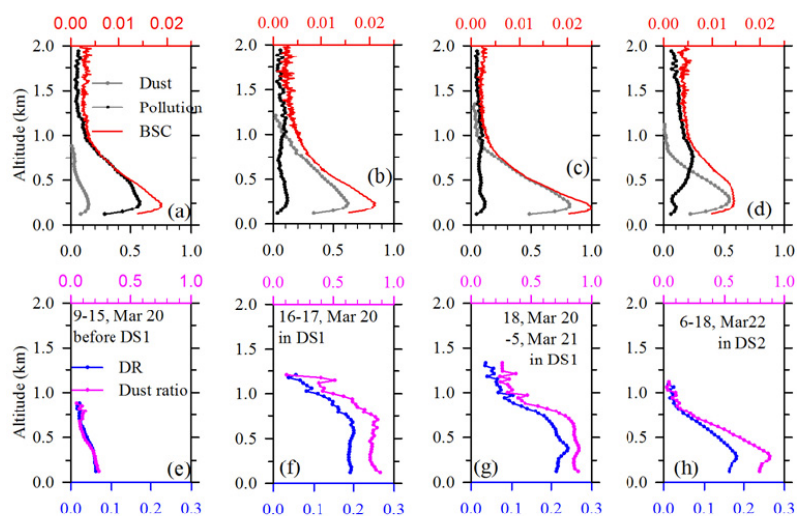
1068

1069

1070   Fig.8 Vertical profiles of the average extinction coefficients of dust and pollution

1071   particles (km^{-1}), attenuated backscattering coefficient (BSC, $sr^{-1}km^{-1}$), depolarization

1072   ratios (DR, unitless), and the ratio of the dust extinction in the total extinction (Dust

1073   ratio, unitless) in four periods of 9:00 - 15:00 of March 20 (before DS1), 16:00 -

1074   17:45 of March 20 (before the highest PM_{10} concentration in DS1), 18:00 of March

1075   20 - 04:45 of March 21 (during the highest PM_{10} concentration in DS1), and 6:00 -

1076   18:00 of March 22 in DS2.

1077

1078

1079

1080
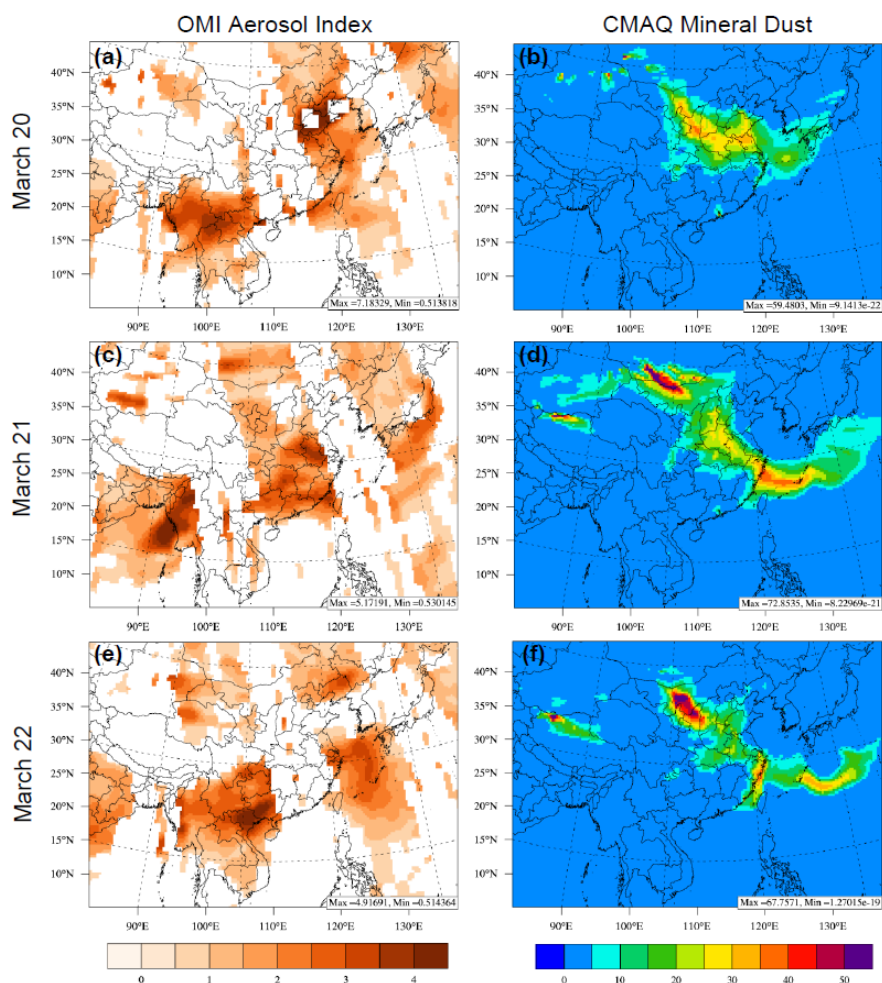
Fig. 9. The spatial distribution of OMI Ultraviolet Aerosol Index (unitless) and simulated mineral aerosols ($\mu g m^{-3}$) from March 20 – 22, 2010, respectively.
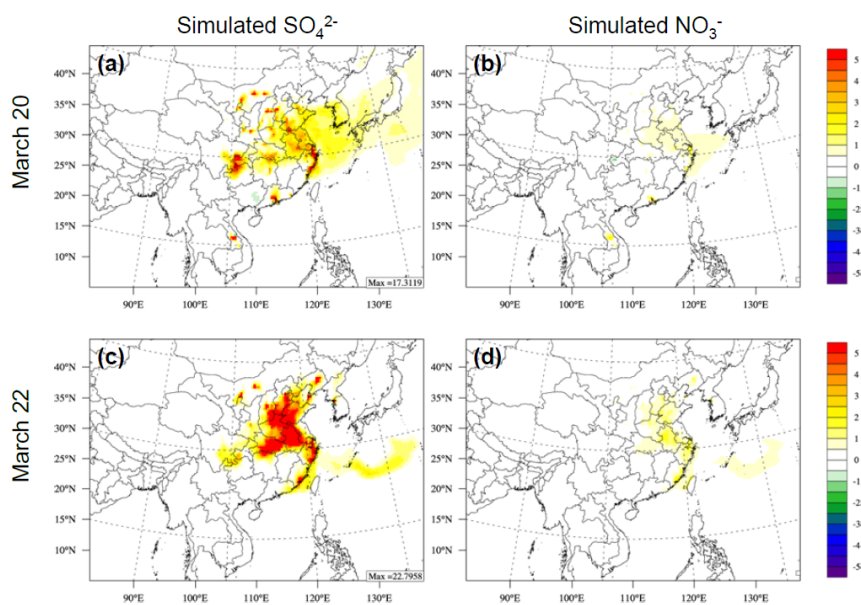
Fig. 10. Simulated SO_4^{2-} and NO_3^- ($\mu g/m^3$) from dust heterogeneous reactions during DS1 and DS2.